Nanoscale

PAPER

View Article Online
View Journal | View Issue

Cite this: *Nanoscale*, 2025, **17**, 19794

Engineering Pb-free relaxor ferroelectric thin films for low voltage energy storage applications

Duarte J. M. Ribeiro,†[a,b] Surya K. P. Nair,†[a,b] Ampattu R. Jayakrishnan,*[a,b] João Oliveira,[a,b] Grégoire Magagnin,[c] David Albertini,[d] Yann Walter,[e] Koppole C. Sekhar,[f] J. Agostinho Moreira,[e] Bernardo G. Almeida,[a,b] Brice Gautier,[d] Bertrand Vilquin,[c] Luís Marques,[a,b] Mario Pereira[a,b] and José P. B. Silva *[a,b]

Pulsed power technologies demand dielectric capacitors that possess a high energy storage density and efficiency at low applied electric fields/voltages. In this work, we engineered the morphology of lead-free $0.85[0.6Ba(Zr_{0.2}Ti_{0.8})O_3–0.4(Ba_{0.7}Ca_{0.3})TiO_3]–0.15SrTiO_3$ (BZCT–STO) epitaxial thin films, fabricated using the pulsed laser deposition technique. Through control of the annealing time, we observed both grain shape and size changes, which induced a change in the relaxor behaviour of the BZCT–STO films. The enhanced relaxor behaviour, assigned to the formation of polar nanoregions, was achieved in the film with uniform smaller spherical grains, which is relevant for improved energy storage performance at low electric fields. The dependence of the electric field on the ferroelectric and energy storage properties of the BZCT–STO thin films was investigated. It is found that the LSMO/BZCT–STO/Au capacitor with enhanced relaxor behaviour shows the optimum energy storage performance, attributable to a moderate maximum polarization and remanent polarization difference, and the highest electric breakdown field. An energy storage density of 9.24 J cm^{-3} with an efficiency of 86.4% at an applied electric field of 1500 kV cm^{-1} was obtained. The increased energy storage density and efficiency in these BZCT–STO thin film capacitors at a low electric field make them one of the most promising systems reported in the literature for energy storage applications. The results reported here clearly evidence the significant impact of the film morphology on the dielectric, ferroelectric and energy storage properties.

Received 13th June 2025,
Accepted 27th July 2025

DOI: 10.1039/d5nr02537k

rsc.li/nanoscale

1. Introduction

Energy storage (ES) plays a crucial role in a sustainable and reliable energy future. Dielectric capacitors, with their ultrafast charging/discharging, high power density, excellent thermal stability, and long lifespan, are promising solutions for pulsed power technology (PPT), which has potential applications in military and defence systems, health, scientific research and industrial applications.[1–4] Although commercial electrostatic capacitors rely on biaxially oriented polypropylene (BOPP), its low energy storage density (ESD) (<7 J cm^{-3}), efficiency (70–90%), and high operating voltage (2–7 MV cm^{-1}) restrict its applicability in low-power devices.[5–7] Multi-layered ceramic capacitors (MLCCs) offer moderate ESD, fast charge/discharge times, and high temperature stability;[2,8,9–12] however, their integration into miniaturized electronic circuits remains limited due to their complexity and moderate performance.[13,14] These challenges underscore the urgent need for dielectric thin films that combine high energy density and efficiency at low electric fields, enabling miniaturized energy storage solutions.

On the other hand, ES thin film capacitors offer other advantages such as high-frequency performance, endurance, thermal stability, and low leakage current.[15] However, achieving high ESD often requires the application of very high electric fields/voltages, typically much higher than 3000 kV cm^{-1} (30 V), this being a serious concern when it comes to their

[a]*Physics Center of Minho and Porto Universities (CF-UM-UP), University of Minho, Campus de Gualtar, 4710-057 Braga, Portugal. E-mail: josesilva@fisica.uminho.pt, jayakrishnan0007@gmail.com*
[b]*Laboratory of Physics for Materials and Emergent Technologies, LaPMET, University of Minho, 4710-057 Braga, Portugal*
[c]*Ecole Centrale de Lyon, INSA Lyon, CNRS, Université Claude Bernard Lyon 1, CPE Lyon, INL, UMR5270, 69130 Ecully, France*
[d]*University Lyon, INSA Lyon, CNRS, Ecole Centrale de Lyon, Université Claude Bernard Lyon 1, CPE Lyon, INL, UMR5270, 69621 Villeurbanne, France*
[e]*IFIMUP – Institute of Physics for Advanced Materials, Nanotechnology and Photonics, Department of Physics and Astronomy, Faculty of Sciences of University of Porto, Rua do Campo Alegre, 687, 4169-007 Porto, Portugal*
[f]*Department of Physics, School of Basic and Applied Science, Central University of Tamil Nadu, Thiruvarur-610 005, India*
†These authors contributed equally to this work.

integration in portable, wearable, and flexible electronics.[2] Therefore, the search for high ESD and efficiency values at low electric fields stimulates research into dielectric films, especially for high-power electronics that prioritize safety, reliability, and minimal insulation costs.[16] This increases the demand for ES capacitors with good ESD and η at low electric fields/voltages, typically up to 2000 kV cm^{-1} (20 V). For instance, 0.93Pb($Mg_{1/3}Nb_{2/3}$)O_3–0.07$PbTiO_3$ thin film capacitors are able to achieve an ESD value of 48.9 J cm^{-3} with an η value of 77.4% at an applied electric field of 2000 kV cm^{-1}.[17] However, lead-based capacitors should be avoided due to their environmental effects and the toxicity of Pb.[18] In this regard, lead-free relaxor ferroelectric (RFE) thin films are considered as promising materials to be used in low electric field ES applications. In recent works, it was demonstrated that 0.5Ba($Zr_{0.2}Ti_{0.8}$)O_3–0.5($Ba_{0.7}Ca_{0.3}$)TiO_3 (BZCT) thin films can exhibit an ESD value of up to 64.8 J cm^{-3} with an η value below 75 69% at an applied electric field of 2000 kV cm^{-1}.[19,20] While a high ESD can be achieved in this material at low applied electric fields, the η value is still below 75%. Therefore, there is a need to achieve a compromise between high ESD and η.

Here, we report an unprecedented high η value with a moderate ESD value, comparable to the one achieved in commercial BOPP capacitors, at low electric fields/voltages, in a lead-free RFE BZCT-based thin film. The result was achieved by incorporating paraelectric $SrTiO_3$ (STO) in a solid solution of 0.6Ba($Zr_{0.2}Ti_{0.8}$)O_3–0.4($Ba_{0.7}Ca_{0.3}$)TiO_3 to form 0.85[0.6Ba($Zr_{0.2}Ti_{0.8}$)O_3–0.4($Ba_{0.7}Ca_{0.3}$)TiO_3]–0.15$SrTiO_3$ (BZCT–STO). We found that the incorporation of STO enhances the ES performance of BCZT ceramics and polycrystalline thin films.[21,22] However, the η value remains below 75%. Therefore, further optimization is required. Here, the morphology of the BZCT–STO epitaxial thin films grown by pulsed laser deposition (PLD) was tuned by changing the annealing time, having a strong impact on the relaxor behaviour and consequently on the ferroelectric and ES properties of the BZCT–STO thin film capacitors. We demonstrate that the epitaxial BCZ–STO thin film capacitors, while exhibiting similar efficiency, show a superior ESD value of 9.24 J cm^{-3} at 1500 kV cm^{-1}, which is 10 times higher than that achieved in ceramic capacitors.[21] Furthermore, the ESD value is ~50% higher than that achieved with polycrystalline films, while the efficiency is 15% higher.[22] The physical mechanism behind the enhanced ferroelectric and ES behaviour is explained in terms of the grain size, uniformity of the film, relaxor behaviour and formation of weakly coupled polar nano regions (PNRs).

2. Experimental procedure

The BZCT–STO target, used for thin film growth by PLD, was prepared using the procedure reported in ref. 21. Before depositing the BZCT–STO thin film, a bottom 15 nm thick $La_{0.67}Sr_{0.33}MnO_3$ (LSMO) electrode was deposited on an STO (100) substrate. The LSMO bottom electrode layer was grown by PLD using an excimer laser (λ = 248 nm) with a laser energy of 300 mJ and a frequency of 3 Hz, at 750 °C. An oxygen partial pressure (pO_2) of 0.1 mbar was used. Then, BZCT–STO thin films with a thickness of ~200 nm were grown without breaking the vacuum with a laser energy of 350 mJ at a temperature of 750 °C. The pulse frequency of the laser was selected at 2 Hz and a pO_2 of 0.05 mbar was used. After the deposition, the films were annealed at 775 °C in a pO_2 of 0.1 mbar at Δt_{anneal} values of 10, 20, 30 and 60 minutes. For simplicity the samples are labelled as @10 min, @20 min, @30 min and @60 min, respectively.

The structural properties of the BZCT–STO layer were investigated by X-ray diffraction using a Bruker D8 Discover diffractometer with Cu-Kα radiation (λ = 1.54056 Å). The morphology of the films was evaluated by scanning electron microscopy (SEM) using a FEI NOVA NanoSEM 200. Grain size statistics were performed by measuring a total of 50 grains.

For electrical measurements, top circular gold (Au) electrodes with 0.25 mm diameter were grown by thermal evaporation using a metal shadow mask patterning. The complex permittivity, expressed as $\varepsilon = \varepsilon' - i\varepsilon''$, where ε' and ε'' are the real (dielectric permittivity) and imaginary parts, respectively, can be calculated from the measured capacitance (C) and loss tangent ($\tan\delta$) using the following equations:[23]

$$C = \varepsilon' \varepsilon_0 \frac{A}{d} \quad (1)$$

$$\tan\delta = \frac{\varepsilon'}{\varepsilon''} \quad (2)$$

where d represents the film thickness, A denotes the electrode area, and ε_0 is the vacuum permittivity. The temperature-dependent dielectric measurements were performed in the 100 Hz to 1 MHz frequency range from room temperature up to 200 °C at a temperature increase rate of 0.5 °C min^{-1}. This was achieved using a PL 706 PID (Polymer Laboratories, Thermal Sciences, Epsom, UK) controller and furnace for precise temperature control. The temperature was monitored using a PT100 resistance thermometer model 1PT100FR828 (Omega, Manchester, UK) and the voltage was measured using a voltmeter model 182 (Keithley, Cleveland, OH, USA). Shielded test leads were utilized to eliminate parasitic impedances from the connection cables.

Ferroelectric hysteresis loops (P–E) were measured with a modified Sawyer–Tower circuit using a sinusoidal signal at a frequency of 1 kHz. The capacitance–electric field (C–E) characteristics were measured using a precision inductance, capacitance and resistance (LCR) meter Agilent E4980A at an AC voltage of 50 mV in the 100 Hz to 1 MHz frequency range.

Piezoresponse force microscopy (PFM) was performed at the nanoscale using a Dimension ICON complete with a Zurich Instruments HF2LI system working in dual-frequency resonance tracking (DFRT) mode.[24] Pt–Ir coated tips were used with a stiffness of between 1 and 10 N m^{-1}. Moreover, DFRT-PFM[25] was performed using an NT-MDT NTEGRA microscope to obtain piezoelectric hysteresis loops at the nanoscale. DFRT-PFM was implemented with Pt–Ir-coated tips at the first

resonance contact frequency ($f \approx 350$ kHz contact). A sequence of low-voltage in-field DC reading triangle signals was applied *via* the bottom electrode to record the piezoresponse.[26]

3. Results and discussion

3.1 Morphological properties

Fig. 1(a–d) shows SEM images of the surface morphology of the BZCT–STO thin films annealed at different times (Δt_{anneal}). In addition, the inset in each image displays the grain size histogram of each sample. It is possible to conclude that the grain size increases with increasing annealing time. We can clearly observe that the grain size increases with increasing annealing time, as shown in the histograms of Fig. 1(a)–(d), which can be attributed to the coalescence process and Ostwald ripening mechanism.[27,28] Besides that, the shape of the grains changes from spherical to squared, which is in agreement with the grain shape evolution as a function of grain size reported in the literature through phase field simulations.[29] This is attributed to atomic diffusion, grain boundary migration, and the minimization of surface and interface energies.[30,31] Similar shape behaviour change was observed in other oxide thin films.[32] During the grain shape evolution, it is possible to observe that the sample annealed for 30 minutes exhibits a mixed behaviour where spherical and squared shapes coexist, which can cause a broader distribution of grain size, as observed in the figure. Moreover, in the case of the sample annealed for 10 minutes, although its surface is atomically smooth with small grain sizes, it also presents bulk-like 0.3–1 μm sized particulates on top, as shown in Fig. S1(a). The appearance of such particulates is common in oxide thin films grown by PLD.[33] However, further increase of the annealing time up to 20 min significantly decreases the number of these particulates (Fig. S1(b)) and also increases the grain size. It has been reported in the current literature that thermodynamically unstable surface irregularities and roughness are significantly decreased as the annealing time increases.[34–37] This is a consequence of atomic diffusion due to a longer time interval at high temperatures, increasing the atomic rearrangement and improving the surface morphology and homogeneity, and also promoting an increase in grain size.[34–36]

In addition, all the samples have the same composition, since they were grown under the same conditions. Fig. S3 shows a representative EDS spectrum of all the samples. In this case, the sample used is the one annealed for 20 minutes. It is possible to observe the presence of all the chemical

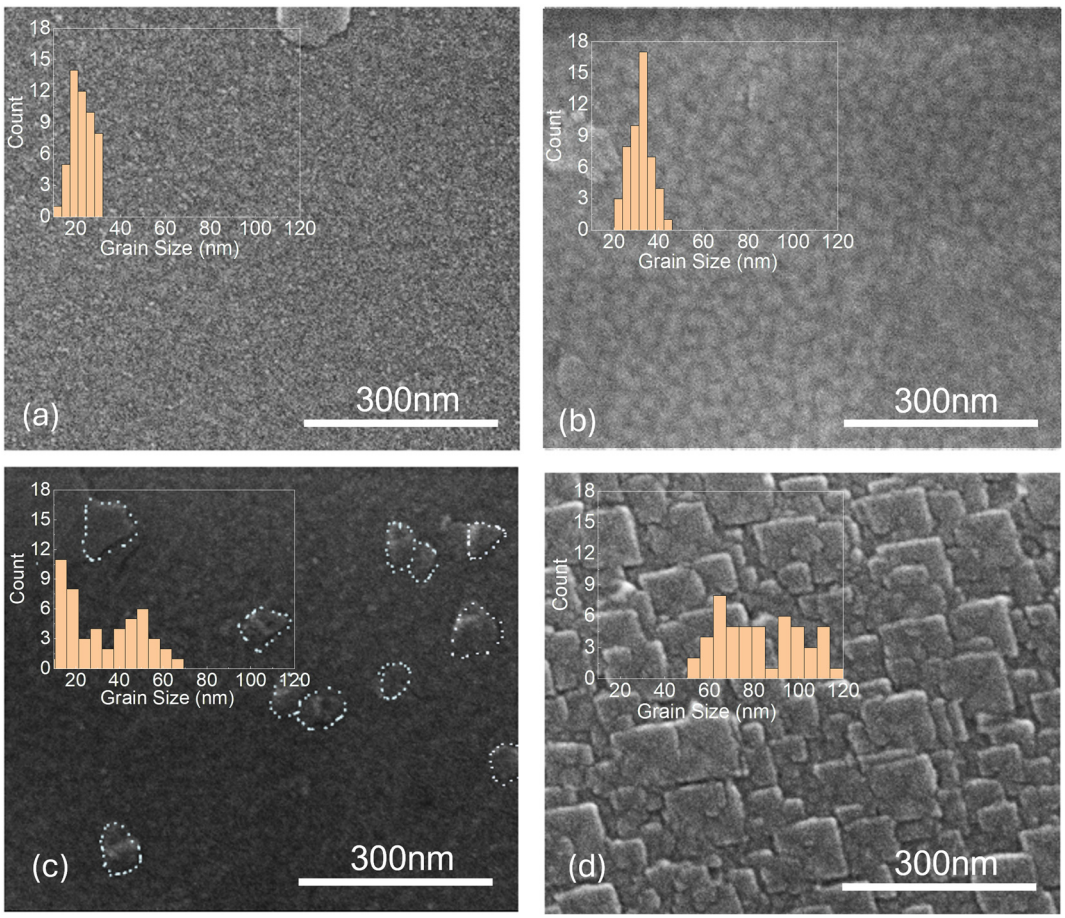

Fig. 1 (a)–(d) Scanning electron microscopy images of the BZCT–STO thin films annealed for 10, 20, 30 and 60 minutes. The insets show the grain size histogram for each sample.

elements from the BCZT–STO film, the LSMO electrode and the STO substrate. However, it was not possible to estimate the stoichiometric composition, given that some of these elements are also present in the substrate and the bottom electrode.

3.2 Dielectric properties

After addressing the changes in film morphology with the annealing time, Δt_{anneal}, we performed dielectric characterization to unravel the role of the annealing time in the relaxor behaviour of the films. Fig. 2(a–d) displays the temperature dependence of the ε' and $\tan\delta$ of the BZCT–STO thin films as a function of Δt_{anneal}, measured at different frequencies ranging from 100 Hz to 1 MHz. At room temperature and at 100 kHz, the ε' values for the BZCT–STO thin films are found to be 420, 139, 93, and 253 for the samples annealed for 10, 20, 30, and 60 minutes, respectively. As the annealing time increases from 10 to 20 minutes, the ε' value of the BZCT–STO thin film decreases. This is likely due to the disappearance of the micron sized particulates. Typically, larger grains tend to enhance the ε' value.[38] Despite the formation of some larger grains, with mean linear dimensions in the 40–60 nm range, the influence of the particulate reduction still dominates when the annealing time increases from 20 to 30 minutes, which causes a further decrease in the ε' value. Further increase in the annealing time up to 60 minutes leads to an increase in the grain size, and consequently, the value of ε' again increases.[39] Furthermore, SEM images reveal a significant change in the grain boundary density as the annealing time increases from 10 to 60 minutes. The lowest values of ε' for the samples annealed at 20 and 30 minutes may be ascribed to the contribution from the low permittivity non-ferroelectric grain boundary (GB) layers. These GB layers will act as dead layers, showing a significant reduction in the dielectric permittivity.[40] In addition, the observed increase in the ε' and $\tan\delta$ values with temperature are related to the conductivity of the films, which makes determination of the temperature phase transition more challenging.[19] However, an anomalous broad peak in the temperature dependence of ε' near 100 °C, associated with the tetragonal to cubic phase transition,[21] is observed in all the BZCT–STO films. This broad behaviour may be attributed to the degree of diffuseness (DPT) and can be quantified using the modified Curie–Weiss law:[41]

$$\frac{1}{\varepsilon'} - \frac{1}{\varepsilon_m} = \frac{(T - T_m)^\gamma}{C}, \quad 1 \le \gamma \le 2,\ T > T_m \tag{3}$$

where ε_m is the dielectric permittivity maximum and T_m its corresponding temperature. The constants γ and C characterize the diffuseness of the phase transition. For a typical ferroelectric, γ is 1, while for an ideal relaxor ferroelectric, γ is 2. Fig. 2(e) shows the plot of $\ln(1/\varepsilon' - 1/\varepsilon_m)$ *versus* $\ln(T - T_m)$; at 100 kHz, the slope value is γ. The values were found to be 1.18 ± 0.02, 1.74 ± 0.01, 1.64 ± 0.02 and 1.58 ± 0.03 for the samples annealed for 10, 20, 30 and 60 minutes, respectively.

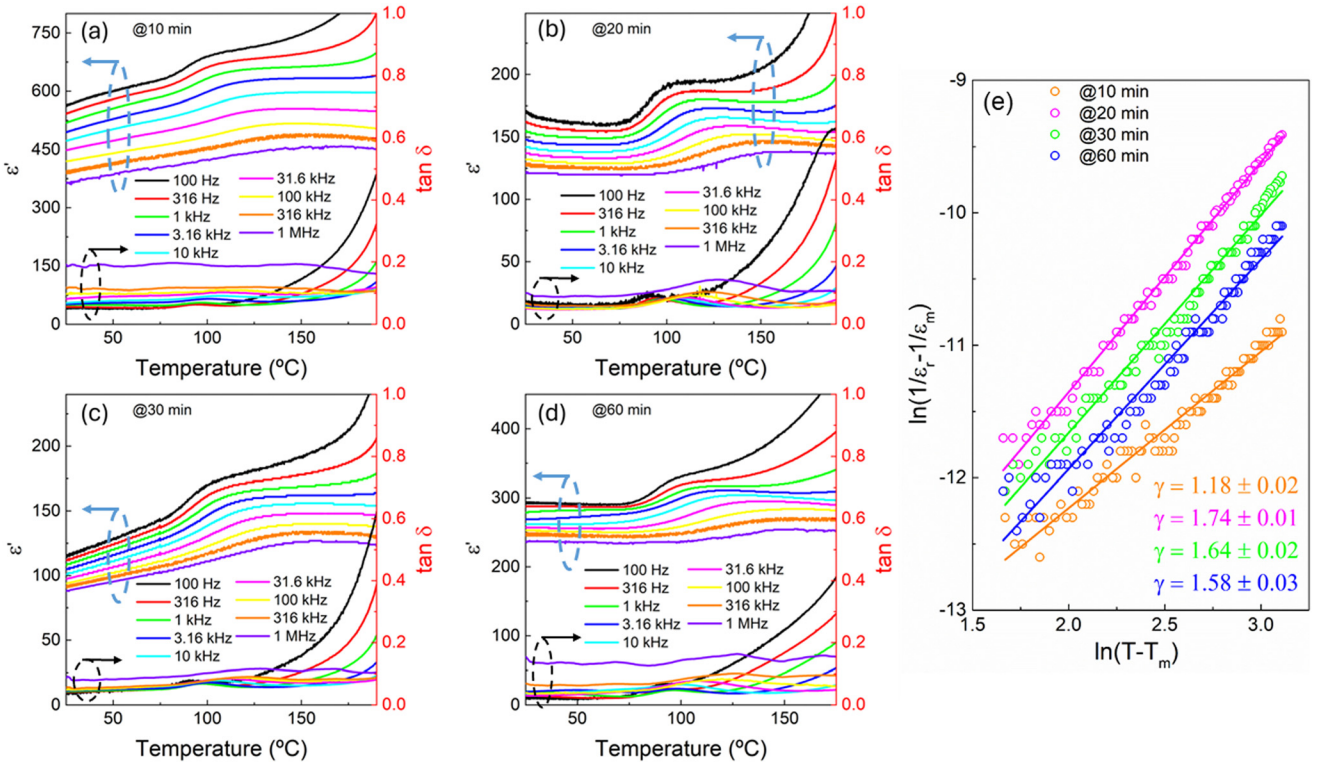

Fig. 2 (a)–(d) Temperature (T)-dependent ε_r and $\tan\delta$ values of the BZCT–STO thin films annealed for 10, 20, 30, and 60 minutes, measured at frequencies ranging from 1 kHz to 1 MHz. (e) Logarithmic plot of $(1/\varepsilon_r - 1/\varepsilon_m)$ *versus* $(T - T_m)$ for the BZCT–STO films annealed for 10, 20, 30, and 60 minutes, measured at 100 kHz.

As the annealing time increases from 10 to 20 minutes, there is an increase in the γ value from 1.18 to 1.74, indicating a higher degree of relaxor behaviour. This is consistent with the SEM analysis, which shows the decrease in the number of bulk-like particulates, the gradual increase of the grain size and the mixing of different grain sizes during this process, which causes the dielectric behaviour to be dominated by the controlled fine structure of the thin film.[42] In the sample annealed @10 min, the large particulates present a bulk-like ferroelectric behaviour, with a corresponding low γ value. As the annealing time increases, the particulate reduction and formation of local grains with increasing annealing time are ascribed to the formation of PNRs.[43,44] This increases the interface number, which prevents the domain wall motion and hinders the long-range ferroelectric order in the @20 min and @30 min films. However, further increase in the annealing time up to 60 minutes leads to the formation of larger grains, resulting in a lower γ value and consequently in a loss of the relaxor behaviour.

3.3 Ferroelectric and energy storage properties

Fig. 3(a–d) illustrates the room temperature polarization–electric field (P–E) hysteresis loops of the BZCT–STO thin films annealed with different times under different applied electric fields. Samples annealed at different times exhibit different P–E loops shapes. As the annealing time increases from 10 to 20 minutes, the loop becomes slimmer, demonstrating an enhanced relaxor ferroelectric behaviour. This is in good agreement with the previously mentioned dielectric studies that show an increased γ value. The relaxor behaviour is ascribed to the formation of PNRs that can be reoriented from the original state swiftly when the applied electric field is removed.[45] As a result, a low remanent polarization (P_r) is achieved. However, the sample annealed for 10 minutes has a higher maximum polarization (P_{max}), when compared to the sample annealed for 20 minutes due to the higher amount of the bulk-like particulates. This result follows the theoretical models that predict a decrease of electric polarization as a consequence of the

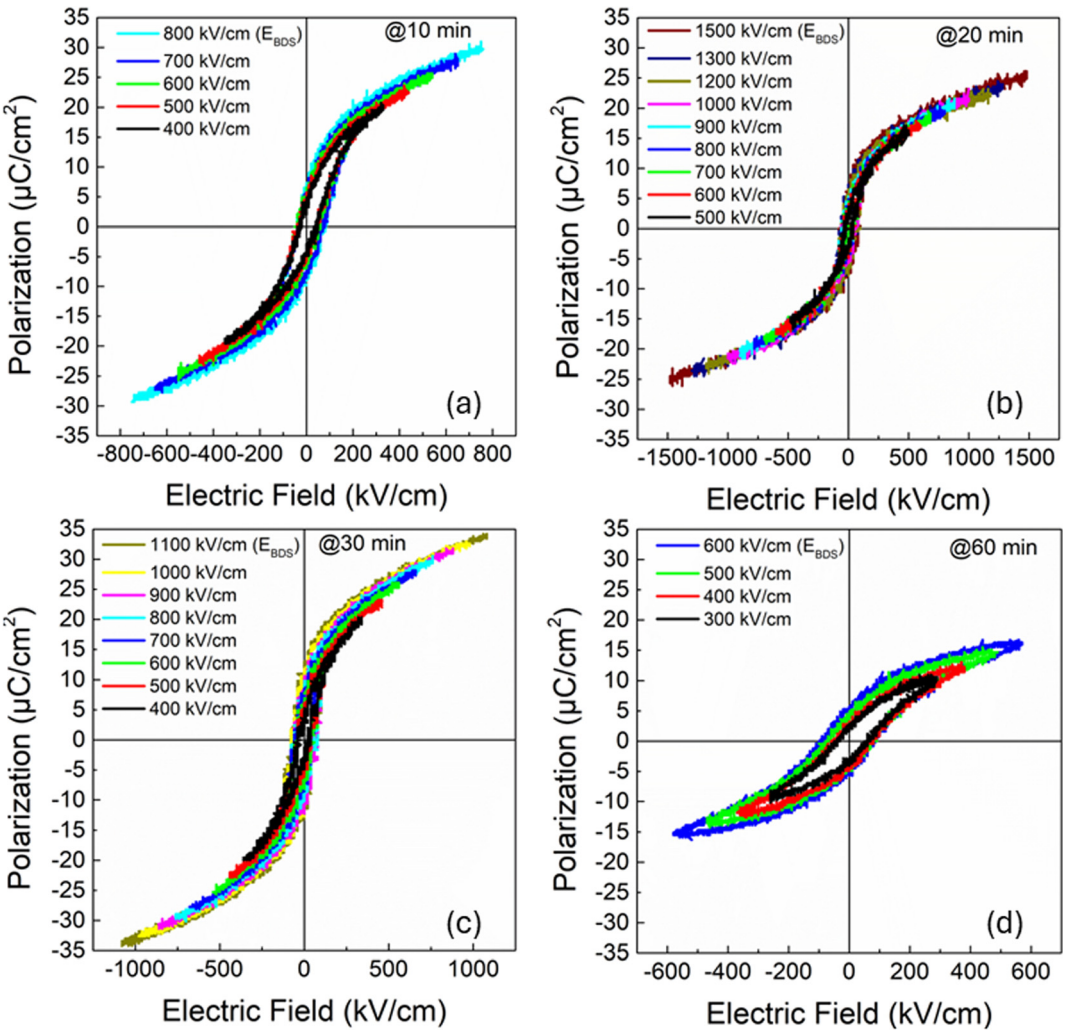

Fig. 3 (a)–(d) P–E plots of the BZCT–STO thin films annealed for 10, 20, 30, and 60 minutes at different electric fields.

grain size decrease.[46] The optimal polarization, P_{max}, is achieved in the sample annealed for 30 minutes. This is due to the co-existence of PNRs and larger grains in the 40–60 nm range that can be seen as ferroelectric domains. Given that the PNRs are polarized at lower external applied electric fields, they induce charge accumulation at the phase boundaries, creating an internal electric field at the ferroelectric domains, leading to an increase in the P_{max} value.[47] However, once the field is withdrawn, the PNRs quickly revert to their random orientations, resulting in a low P_r value and a slim P–E loop.

The increase in the annealing time up to 60 minutes leads to a broadening of the P–E loop due to the increased grain size, as observed in SEM analysis. In addition, the maximum low applied electric field in this sample, as well as its variation in all the samples, will be further discussed later. Given that the sample annealed for 20 minutes shows the most promising ferroelectric behaviour for ES, we have performed capacitance–electric field (C–E) and PFM measurements to confirm its RFE behaviour.

Fig. S2(a) shows the electric field dependence of the C–E curves for the film annealed for 20 min. It is possible to observe the typical butterfly feature of ferroelectric behaviour. In addition, the coercive field (E_c) is estimated to be 25 kV cm^{-1}, irrespective of the electric field used. This value is lower than the one estimated from the P–E loops (~70 kV cm^{-1}) due to the fact that C–E measurement is a quasi-static process, while the P–E loop is a dynamic one.[48] The frequency-dependent C–E curve for the film annealed at 20 min in the range 1–100 kHz is plotted in Fig. S2(b) and it is possible to confirm that the C–E curves are stable across a wide frequency range. This suggests that the influence of defects on the polarization reversal process is negligible.[49]

The ferroelectric and polar domain structures were further investigated by PFM. Fig. 4(a) shows the surface topography of the BZCT–STO film annealed for 20 minutes. The surface is smooth and the average grain size is ~30 nm, which are consistent with the grain size distribution obtained from the SEM analysis. Piezoresponse amplitude and phase scans, as shown in Fig. 4(b) and (c), respectively, reveal distinct contrast regions that exhibit some correlation with the topography. The hysteretic dependency of the amplitude and phase piezo-signals on the applied bias electric field is shown in Fig. 4(d) and clearly reveals well-defined, reversible, and reproducible cycles, corroborating the polar nature of the BZCT–STO films. The cycles have a +1 V offset with coercive fields set at +0.4 and +1.4 V. This asymmetry between the negative and positive bias fields could be partially due to the difference in work functions between the bottom (LSMO) and top (Pt–Ir) electrodes.[50,51] The critical electric field E_c, using a parallel plate capacitor approximation, was estimated to be ~25 kV cm^{-1}, which is in good agreement with the value obtained from the C–E measurements. By writing at +2.5/−0.5 V DC and reading with

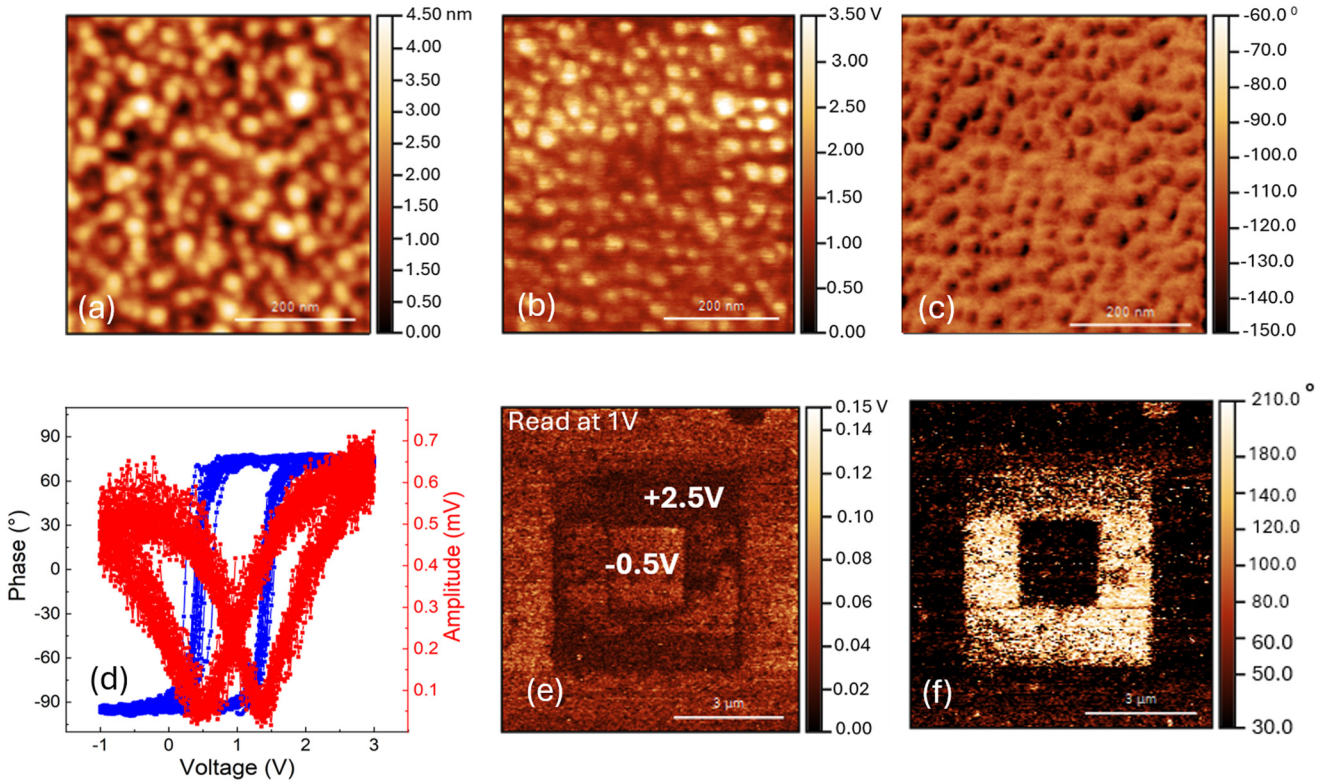

Fig. 4 (a) Topography image with respective out-of-plane piezo-response to (b) amplitude and (c) phase signals. (d) Typical phase and amplitude hysteresis loops. (e) PFM amplitude and (f) phase signals of the domains written with +2.5 V (large square) and −0.5 V (small square) DC biases.

a +1 V DC offset, it becomes possible to observe two polarization states separated by 180° (Fig. 4(e)) and phase (Fig. 4(f)) images. In addition, it is possible to observe some back-switching, typical for the relaxation of domains in RFEs.

To further confirm the high quality of the BZCT-STO film, we performed XRD measurements. Fig. S2(c) shows the XRD pattern of the thin film annealed for 20 min. Besides the XRD (00*l*) diffraction peaks from the STO substrate, it is possible to observe the (00*l*) diffraction peaks from the BZCT–STO film. Moreover, no additional diffraction peaks arising from secondary phases are observed. The out-of-plane lattice parameter of the BZCT–STO layer was calculated to be 4.07 Å, which is higher than that obtained in the bulk BZCT–STO sample (4.00 Å),[21] suggesting the presence of in-plane compressive strains generated by the STO substrate.[52]

Coming back to Fig. 2, it is possible to expect that the BZCT–STO films should exhibit different ES behaviours. The ESD of a capacitor can be calculated using the following equation:[53]

$$\mathrm{ESD} = \int_{P_r}^{P_{max}} E\mathrm{d}P \quad (4)$$

Fig. 5(a) shows the evolution of the ESD as a function of the applied electric field for all the samples. To explain the different behaviours, we have estimated the difference between the maximum and the remanent polarizations ($P_{max} - P_r$, ΔP) for all the samples. Fig. 5(b) shows the ΔP value as a function of the applied electric field for the BZCT–STO thin films annealed for 10, 20, 30, and 60 minutes. The highest ΔP value is achieved for the sample annealed for 10 minutes due to the high P_{max} value, which was already suggested by the highest ε_r value found in the dielectric studies for this sample. However, the ES properties are also dependent on the electric breakdown strength (E_{BDS}). The maximum E_{BDS} value of the BZCT–STO thin films annealed for 10, 20, 30, and 60 minutes at room temperature were found to be 800, 1500, 1100 and 600 kV cm^{-1}, respectively. The enhanced E_{BDS} value observed for the sample annealed for 20 minutes is ascribed to the small and uniform grains that prevent the propagation and growth of electric filaments and trees.[54] This is supported by phase field simulations that demonstrate that uniformity causes enhancement of the dielectric breakdown strength.[55] In addition, the lowest E_{BDS} value is observed for the sample annealed for 60 minutes. This effect is supported by previous local electric field simulation studies,[55] which shows that the presence of these sharp grain boundaries creates regions of high field intensity, leading to increased vulnerability to dielectric breakdown. Besides, the small and uniform grains of the @20 min sample disrupt the long-range ferroelectric order by disturbing the translational symmetry by increasing the grain boundary density.[2] This will promote the accumulation

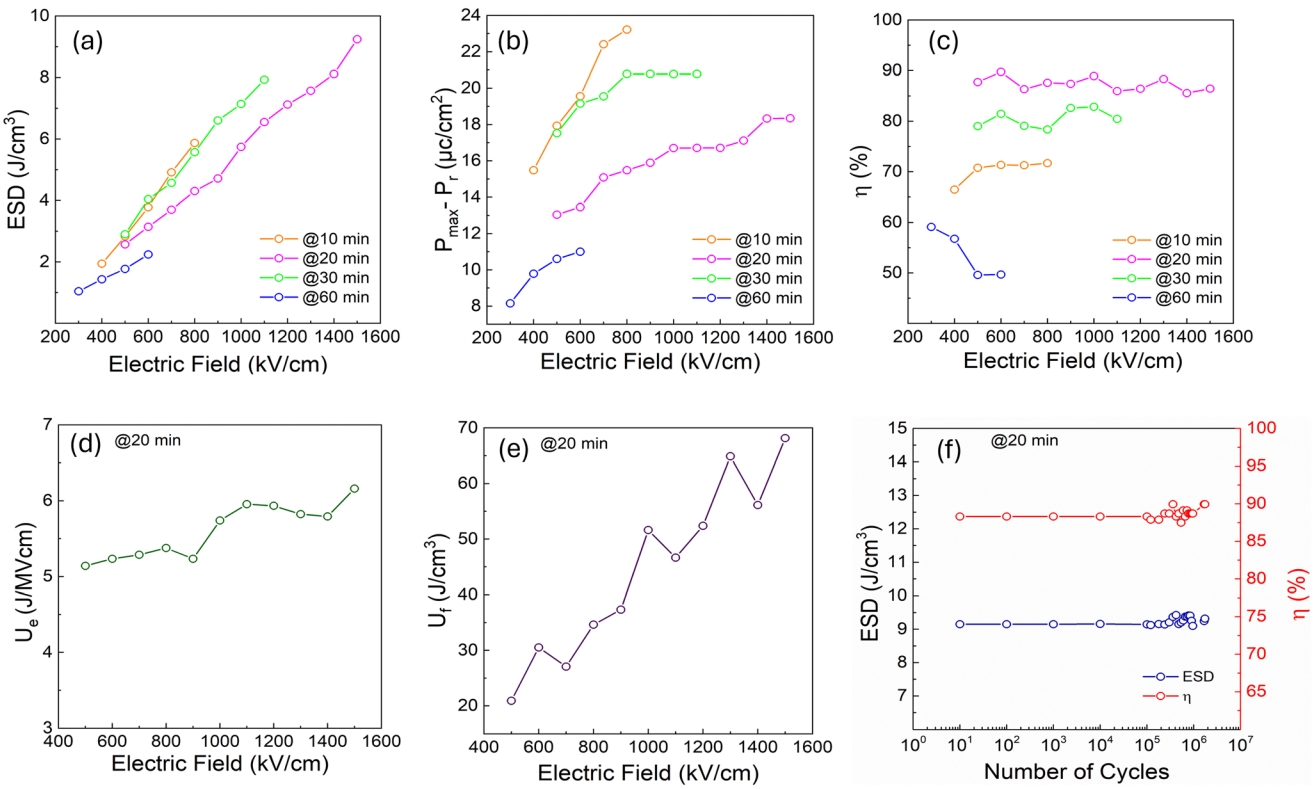

Fig. 5 (a) ESD values, (b) plots of $P_{max} - P_r$ and (c) η values as a function of applied electric field for the samples annealed with different annealing times. (d) U_e and (e) U_f values as a function of the applied electric fields for the sample annealed for 20 minutes. (f) ESD values and η *versus* number of cycles for the sample annealed for 20 minutes.

of moving charges at the grain boundaries. As a result, it provides a barrier effect against the scattering of electrons under an external electric field and thereby enhances the E_{BDS}.[2] Therefore, the highest ES performance was achieved for the sample annealed for 20 minutes due to the moderate ΔP and the highest E_{BDS} values. The η value of the capacitors can be also determined using the following equation:[56]

$$\eta = \left(\frac{\text{ESD}}{\text{ESD} + W_{\text{loss}}}\right) \times 100 \quad (5)$$

where W_{loss} denotes the energy loss incurred during the cycling process. W_{loss} is the area inside the hysteresis loops. Fig. 5(c) shows the dependence of η on the applied electric field for all the samples. Remarkably, the sample annealed for 20 minutes shows $\eta \geq 85\%$ for all the applied electric fields. This value is much higher than the one found in previous works for BZCT-based ES capacitors operating at low applied electric fields.[19,20] In addition, it is possible to observe that the η value follows a pattern similar to the one observed for the γ parameter, suggesting that the relaxor behaviour and the formation of PNRs dictate the capability of the BZCT–STO film to store the energy efficiently. The capability of the material to store a high ESD under a specific electric field can be evaluated as follows:[16]

$$U_e = \frac{\text{ESD}}{\text{Electric field}} \quad (6)$$

Fig. 5(d) shows the evolution of U_e as a function of the applied electric field for the sample annealed for 20 minutes. It is possible to observe that a maximum U_e value of 6.16 J MV cm^{-1} is achieved for an applied electric field of 1500 kV cm^{-1}. In addition, the quantitative evaluation of the trade-off between the high ESD and η values can be evaluated as follows:[16]

$$U_f = \frac{\text{ESD}}{(1-\eta)} \quad (7)$$

Fig. 5(e) shows the variation of U_f as a function of the applied electric field for the sample annealed for 20 minutes. A maximum of 68.14 J cm^{-3}, for an applied electric field of 1500 kV cm^{-1}, was achieved. The capability of charging/discharging with cycling was evaluated and Fig. 4(f) shows the evolution of the ESD and η as a function of the number of cycles for the sample annealed for 20 minutes. It is possible to conclude that this samples shows a fatigue-free behaviour up to $\sim 10^6$ cycles, confirming the potential of these capacitors for energy storage applications at low electric fields.

Table 1 compares the performance of the present ES capacitor with those reported in the literature for lead-based and lead-free RFE thin films under low applied electric fields/voltages. Compared to lead-based RFE thin films, our capacitor shows a smaller U_e value and a comparable U_f value. However, the toxicity of Pb hinders these materials' practical application. When compared to $BiFeO_3$-based and $(Na_{0.5}Bi_{0.5})TiO_3$-based capacitors, our capacitor exhibits also a significantly lower U_e value. This is due to the fact that these materials usually exhibit higher P_{max} values, which in the end result in higher ΔP and enhanced ESD values. However, the main drawback of these materials is the presence of highly volatile elements such as Bi and Na, which hinders the possibility of replacing Pb-based thin films.[48] When compared to previous works in BZCT film capacitors, our thin film capacitors show comparable U_e

Table 1 Comparison of ES performances at low electric fields of the present capacitors with the most relevant lead-based and lead-free relaxor ferroelectric thin films and ceramics reported in the literature and measured at room temperature

Capacitor	Thickness (nm)	E (kV cm^{-1})	Applied voltage (V)	Frequency (kHz)	ESD (J cm^{-3})	η (%)	U_e (J MV cm^{-2})	U_f (J cm^{-3})	Ref.
Lead-based RFE thin films									
$SrTiO_3$/67Pb($Mg_{1/3}Nb_{2/3}$)O_3–33$PbTiO_3$-PbO-MgO/Au	500	500	25	1	8.16	85.8	16.3	57.5	16
SRO/$Pb_{0.9}La_{0.1}Zr_{0.52}Ti_{0.48}O_3$/SRO	200	400	8	1	5.5	90.3	13.7	56.7	57
SRO/$PbHfO_3$/SRO	75	1240	9.3	10	21	90.0	17.0	210.0	58
Lead-free RFE thin films									
Pt/0.5($Bi_{0.5}Na_{0.5}$)TiO_3–0.5Bi($Zn_{0.5}Zr_{0.5}$)O_3/$LaNiO_3$	700	1500	105.0	—	40.8	64.1	27.2	113.0	47
ITO/$Na_{0.5}Bi_{0.5}Ti0._{97}Ni_{0.03}O_3$/Au	300	500	15.0	10	14.8	49.0	29.6	29.0	59
Pt/$Na_{0.5}K_{0.5}NbO_3$/$BiMnO_3$ /Au	700	861	60.3	—	11.42	79.7	13.2	56.8	60
Pt/0.68$BiFeO_3$–0.32$BaTiO_3$/Si	200	900	18.0	1	19	51.0	21.1	38.8	61
Pt/0.7($Na_{0.5}Bi_{0.5}$)TiO_3–0.3$SrTiO_3$/Pt	190	1895	36.0	1	27	41.0	14.2	45.8	62
Pt/$Bi_{0.5}$($Na_{0.8}K_{0.2}$)$_{0.5}TiO_3$–0.10$BiFeO_3$/Au	800	1200	96.0	1	22.12	60.8	18.4	56.4	63
Pt/0.72$Bi_{0.5}Na_{0.5}TiO_3$–0.18$Bi_{0.5}K_{0.5}TiO_3$–0.10$SrTiO_3$–1.0Fe/Au	900	1100	99.0	0.10	20.34	65.2	18.4	58.4	64
Pt/$Bi_{0.5}Na_{0.5}Ti_{0.9}Mn_{0.1}O_{3-\delta}$/Pt	171	1404	24.0	1	19.84	34.0	14.1	30.1	65
Pt/$SrTiO_3$/$(BiFeO_3)_{0.4}$–$(SrTiO_3)_{0.6}$/Pt	400	975	39.0	1	18.6	85.0	19.1	124	66
Nb:$SrTiO_3$/$NaNbO_3$–0.04$CaZrO_3$/Pt	300	833	25.0	2	19.64	64.5	23.5	55.3	67
Pt/0.5Ba($Zr_{0.2}Ti_{0.8}$)O_3–0.5($Ba_{0.7}Ca_{0.3}$)TiO_3/Au	120	1167	14.0	1	10	69.0	8.6	32.3	19
LSMO/BZCT–STO/Au	200	1500	30.0	1	9.24	86.4	6.2	68.14	This work

and twice the U_f values. Furthermore, our capacitors exhibit one of the highest U_f values when compared to lead-free RFE thin films. Therefore, this work demonstrates a novel low applied electric field electrostatic ES capacitor that can be used in applications such as smart phones and implantable and wearable electronics.

4. Conclusion

In this work, it was demonstrated that the morphology of 0.85[0.6Ba$(Zr_{0.2}Ti_{0.8})O_3$–0.4$(Ba_{0.7}Ca_{0.3})TiO_3$]–0.15$SrTiO_3$ (BZCT–STO) epitaxial thin films can be controlled by the annealing time, which has a significant impact on the dielectric relaxor behaviour, the ferroelectricity, and the energy storage performance of the films. The LSMO/BZCT–STO/Au capacitor annealed for 20 minutes showed an enhanced relaxor behaviour attributable to its more uniform small grain distribution, which causes an optimum energy storage density of 9.24 J cm^{-3} with an efficiency of 86.4% at an applied electric field of 1500 kV cm^{-1}. In addition, these energy storage characteristics were found to be stable for up to 10^6 cycles. Therefore, through engineering the BZCT–STO thin film microstructure, it was possible to achieve one of the best trade-offs between high energy storage density and efficiency reported in the literature on BZCT-based films, which opens up the possibility of using these capacitors for low applied electric field energy storage applications.

Author contributions

D. J. M. R, S. K. P. and A. R. J. prepared the samples, performed the structural, ferroelectric and energy storage characterization, analyzed the data, and wrote the first draft of the manuscript. J. O. and B. G. A. performed the dielectric characterization and analyzed the data. G. M., D. A., B. G. and B. V. performed the PFM characterization and analyzed the data. Y. W. and J. A. M. performed the CV characterization and analyzed the data. K. C. S. prepared the PLD target and contributed to the data analysis. L. M., M. P. and J. P. B. S. collaboratively designed the experiments and supervised the project. All authors contributed to the data interpretation and the writing and editing of the final manuscript.

Conflicts of interest

The authors declare no conflict of interest.

Data availability

The authors confirm that the data supporting the findings of this study are available within the article and its SI.

Supplementary information is available. See DOI: https://doi.org/10.1039/d5nr02537k

Acknowledgements

This work was supported by (i) the Portuguese Foundation for Science and Technology (FCT) in the framework of the Strategic Funding Contracts UIDB/04650/2020, (ii) the exploratory research projects 2022.01740.PDTC (https://doi.org/10.54499/2022.01740.PTDC), PTDC/NAN-MAT/0098/2020, and 2022.03564.PTDC, and (iii) the project M-ERA-NET3/0003/2021 – NanOx4EStor grant agreement No. 958174 (https://doi.org/10.54499/M-ERA-NET3/0003/2021). J. P. B. S. also thanks FCT for the contract under the FCT Tenure program 1st edition. J. Oliveira acknowledges his Ph.D. grant from FCT with reference SFRH/BD/146886/2019. The authors would like also to thank engineer José Santos for technical support at the Thin Film Laboratory. The authors acknowledge the Consortium Lyon Saint-Etienne de Microscopie (CLYM, FED 4092) for access to the microscopes.

References

1 Z. Yang, H. Du, S. Qu, Y. Hou, H. Ma, J. Wang, J. Wang, X. Wei and Z. Xu, Significantly enhanced recoverable energy storage density in potassium-sodium niobate-based lead-free ceramics, *J. Mater. Chem. A*, 2016, **4**(36), 13778–13785.

2 A. R. Jayakrishnan, J. P. B. Silva, K. Kamakshi, D. Dastan, V. Annapureddy, M. Pereira and K. C. Sekhar, Are lead-free relaxor ferroelectric materials the most promising candidates for energy storage capacitors?, *Prog. Mater. Sci.*, 2023, **132**, 101046.

3 H. Palneedi, M. Peddigari, A. Upadhyay, J. P. Silva, G. T. Hwang and J. Ryu, Lead-based and lead-free ferroelectric ceramic capacitors for electrical energy storage, in *Ferroelectric Materials for Energy Harvesting and Storage*, Woodhead Publishing, 2021, pp. 279–356.

4 S. Li, C. Zhang, S. Li, L. Zhang and H. Wu, Enhanced energy-storage performance with optimized thermally stable dielectric property in BNT–BST ceramics modified by KNN doping, *J. Adv. Dielectr.*, 2024, **14**(3), 2440011.

5 D. Q. Tan, Review of polymer-based nanodielectric exploration and film scale-up for advanced capacitors, *Adv. Funct. Mater.*, 2020, **30**(18), 1808567.

6 T. Zhang, J. Li, M. Wang, H. Chen, S. Zhao, Y. Liu, L. Huang, J. Xu and P. Zhang, Significantly improved high-temperature energy storage performance of BOPP films by coating nanoscale inorganic layer, *Energy Environ. Mater.*, 2024, **7**(2), e12549.

7 M. Ritamäki, I. Rytöluoto and K. Lahti, Performance metrics for a modern BOPP capacitor film, *IEEE Trans. Dielectr. Electr. Insul.*, 2019, **26**(4), 1229–1237.

8 P. Zhao, Z. Cai, L. Chen, L. Wu, Y. Huan, L. Guo, L. Li, H. Wang and X. Wang, Ultra-high energy storage performance in lead-free multilayer ceramic capacitors via a multi-scale optimization strategy, *Energy Environ. Sci.*, 2020, **13**(12), 4882–4890.

9 J. Zhang, W. Li, Y. Chen, X. Wang, M. Huang, T. Liu, Y. Deng, Q. Wu and Z. Li, Dielectric and anti-reduction properties of $BaTiO_3$-based ceramics for MLCC application, *Ceram. Int.*, 2023, **49**(15), 24941–24947.

10 P. Zhao, H. Wang, L. Wu, L. Chen, Z. Cai, L. Li and X. Wang, High-performance relaxor ferroelectric materials for energy storage applications, *Adv. Energy Mater.*, 2019, **9**(17), 1803048.

11 J. Li, F. Li, Z. Xu and S. Zhang, Multilayer lead-free ceramic capacitors with ultrahigh energy density and efficiency, *Adv. Mater.*, 2018, **30**, 1802155.

12 G. Wang, J. Li, X. Zhang, Z. Fan, F. Yang, A. Feteira, D. Zhou, D. C. Sinclair, T. Ma, X. Tan and D. Wang, Ultrahigh energy storage density lead-free multilayers by controlled electrical homogeneity, *Energy Environ. Sci.*, 2019, **12**(2), 582–588.

13 M. Jiang, Z. Peng, Q. Zhou, D. Wu, L. Weiy, P. Liangz, X. Chao and Z. Yang, Superior energy storage performance of BNT-based ferroelectric ceramics based on maintaining high polarization and breakdown strength, *J. Adv. Dielectr.*, 2024, **14**(04), 2340005.

14 Y. Li, N. Fan, J. Wu, B. Xu, X. Li, X. Liu and F. Li, Enhanced energy storage performance in NBT-based MLCCs via cooperative optimization of polarization and grain alignment, *Nat. Commun.*, 2024, **15**(1), 8958.

15 H. Palneedi, M. Peddigari, G. T. Hwang, D. Y. Jeong and J. Ryu, High-performance dielectric ceramic films for energy storage capacitors: progress and outlook, *Adv. Funct. Mater.*, 2018, **28**(42), 1803665.

16 J. Belhadi, Z. Hanani, N. A. Shepelin, U. Trstenjak, N. Daneu, A. M. Müller, C. Vockenhuber, B. Ambrožič, V. Bobnar, G. Koster, M. El Marssi, T. Lippert and M. Spreitzer, Ultra-high energy storage density and efficiency at low electric fields/voltages in dielectric thin film capacitors through synergistic effects, *J. Mater.*, 2025, **11**(5), 100980.

17 Y. Li, J. Xu, Z. Xu, Y. Yu, Y. Zhang, L. Lu, W. Zheng, C. Ding, Z. Wen, H. Shi and C. Lu, Enhanced energy storage properties in relaxor $Pb(Mg_{1/3}Nb_{2/3})O_3$–$PbTiO_3$ thin-film capacitors by incorporating buffer layers, *Appl. Phys. Lett.*, 2022, **120**(25), 252901.

18 X. Tang, Y. Li, J. Zhang, M. Wang, H. Chen, L. Huang and T. Liu, Energy storage properties of samarium-doped bismuth sodium titanate-based lead-free ceramics, *Chem. Eng. J.*, 2023, **473**, 145363.

19 S. W. Konsago, K. Žiberna, A. Matavž, B. Mandal, S. Glinšek, Y. Fleming, A. Benčan, G. L. Brennecka, H. Uršič and B. Malič, Engineering the microstructure and functional properties of $0.5Ba(Zr_{0.2}Ti_{0.8})O_3$–$0.5(Ba_{0.7}Ca_{0.3})TiO_3$ thin films, *ACS Appl. Electron. Mater.*, 2024, **6**(6), 4467–4477.

20 S. R. Reddy, V. V. B. Prasad, S. Bysakh, V. Shanker, N. Hebalkar and S. K. Roy, Superior energy storage performance and fatigue resistance in ferroelectric BCZT thin films grown in an oxygen-rich atmosphere, *J. Mater. Chem. C*, 2019, **7**(23), 7073–7082.

21 A. R. Jayakrishnan, K. V. Alex, K. Kamakshi, J. P. B. Silva, K. C. Sekhar and M. J. M. Gomes, Enhancing the dielectric relaxor behaviour and energy storage properties of $0.6Ba(Zr_{0.2}Ti_{0.8})O_3$–$0.4(Ba_{0.7}Ca_{0.3})TiO_3$ ceramics through the incorporation of paraelectric $SrTiO_3$, *J. Mater. Sci.: Mater. Electron.*, 2019, **30**, 19374–19382.

22 M. Tasneem, C. R. P. Monteiro, N. S. K. Kumar, J. P. B. Silva, K. C. Sekhar, K. Kamakshi and M. Pereira, Thickness-dependent microstructure, resistive switching, ferroelectric, and energy storage properties of pulsed laser deposited $0.85[0.6Ba(Zr_{0.2}Ti_{0.8})O_3$–$0.4(Ba_{0.7}Ca_{0.3})TiO_3]$–$0.15SrTiO_3$ thin films, *Ceram. Int.*, 2023, **49**(12), 20756–20762.

23 J. Oliveira, M. Silva, P. Santos, L. Ferreira and A. Pereira, Structural, magnetic, and dielectric properties of laser-ablated $CoFe_2O_4/BaTiO_3$ bilayers deposited over highly doped Si (100), *Materials*, 2024, **17**(23), 5707.

24 B. J. Rodriguez, C. Callahan, S. V. Kalinin and R. Proksch, Dual-frequency resonance tracking atomic force microscopy, *Nanotechnology*, 2007, **18**, 475504.

25 S. Jesse, A. P. Baddorf and S. V. Kalinin, Switching spectroscopy piezoresponse force microscopy of ferroelectric materials, *Appl. Phys. Lett.*, 2005, **88**(6), 062908.

26 S. Martin, A. Baddorf, G. Jones, L. Davis and M. J. M. Gomes, Interpretation of multiscale characterization techniques to assess ferroelectricity: The case of $GaFeO_3$, *Ultramicroscopy*, 2017, **172**, 47–51.

27 A. R. Jayakrishnan, P. V. K. Yadav, J. P. B. Silva and K. C. Sekhar, Microstructure tailoring for enhancing the energy storage performance of $0.98[0.6Ba(Zr_{0.2}Ti_{0.8})O_3$–$0.4(Ba_{0.7}Ca_{0.3})TiO_3]$–$0.02BiZn_{1/2}Ti_{1/2}O_3$ ceramic capacitors, *J. Sci.: Adv. Mater. Devices*, 2020, **5**(1), 119–124.

28 S. Nie, B. Gao, X. Wang, Z. Cao, E. Guo and T. Wang, The influence of holding time on the microstructure evolution of Mg–10Zn–6.8Gd–4Y alloy during semi-solid isothermal heat treatment, *Metals*, 2019, **9**, 420.

29 S. Choudhury, Y. L. Li, C. Krill and L. Q. Chen, Effect of grain orientation and grain size on ferroelectric domain switching and evolution: Phase field simulations, *Acta Mater.*, 2007, **55**(4), 1415–1426.

30 S.-C. Jeon, J. G. Fisher, S.-J. L. Kang and K.-S. Moon, Grain growth behavior of $0.95(Na_{0.5}Bi_{0.5})TiO_3$–$0.05BaTiO_3$ controlled by grain shape and second phase, *Materials*, 2020, **13**, 1344.

31 F. Fu, J. Zhai, Z. Xu, B. Shen and X. Yao, Grain growth kinetics of textured-$BaTiO_3$ ceramics, *Bull. Mater. Sci.*, 2014, **37**, 779–787.

32 X. Cao, L. Zhi, Y. Li, F. Fang, X. Cui, L. Ci, K. Ding and J. Wei, Fabrication of perovskite films with large columnar grains via solvent-mediated Ostwald ripening for efficient inverted perovskite solar cells, *ACS Appl. Energy Mater.*, 2018, **1**(2), 868–875.

33 N. R. M. Ashfold, F. Claeyssens, G. T. Reilly and N. L. Allan, Pulsed laser ablation and deposition of thin films, *Chem. Soc. Rev.*, 2004, **33**(1), 23–31.

34 Y.-W. Cheng, H.-Y. Wu, Y.-Z. Lin, C.-C. Lee and C.-F. Lin, Post-annealing effects on pulsed laser deposition-grown GaN thin films, *Thin Solid Films*, 2015, **577**, 17–25.

35 S. W. Jiang, Q. Y. Zhang, Y. R. Li, Y. Zhang, X. F. Sun and B. Jiang, Structural characteristics of $SrTiO_3$ thin films processed by rapid thermal annealing, *J. Cryst. Growth*, 2005, **274**(3–4), 500–505.

36 W.-J. Liu, Y.-H. Chang, C.-C. Chiang, Y.-T. Chen, P.-X. Lu, Y.-J. He and S.-H. Lin, Studying the effects of annealing and surface roughness on both the magnetic property and surface energy of $Co_{60}Fe_{20}Sm_{20}$ thin films on Si(100) substrate, *Coatings*, 2023, **13**, 1783.

37 M. Liang, J. Yang, H. Yang, C. Liang, Z. Nie, H. Ai, T. Zhang, J. Ma, H. Huang and J. Wang, Effect of annealing conditions on surface morphology and ferroelectric domain structures of $BiFeO_3$ thin films, *J. Adv. Dielectr.*, 2024, **14**(02), 2440002.

38 Y. Wang, S. Zhang, H. Ma and J. Liu, Colossal permittivity materials as superior dielectrics for diverse applications, *Adv. Funct. Mater.*, 2019, **29**(27), 1808118.

39 R. Zuo, X. Chen, J. Guo and Y. Li, Observation of giant dielectric constant in $CdCu_3Ti_4O_{12}$ ceramics, *Solid State Commun.*, 2006, **138**(2), 91–94.

40 V. Buscaglia, M. T. Buscaglia, M. Viviani, L. Mitoseriu, P. Nanni, V. Trefiletti, P. Piaggio, I. Gregora, T. Ostapchuk, J. Pokorný and J. Petzelt, Grain size and grain boundary-related effects on the properties of nanocrystalline barium titanate ceramics, *J. Eur. Ceram. Soc.*, 2006, **26**(14), 2889–2898.

41 L. R. Moreira and R. P. S. M. Lobo, Phenomenological study of diffuse phase transitions, *J. Phys. Soc. Jpn.*, 1992, **61**(6), 1992–1995.

42 X.-G. Tang and H. L.-W. Chan, Effect of grain size on the electrical properties of $(Ba,Ca)(Zr,Ti)O_3$ relaxor ferroelectric ceramics, *J. Appl. Phys.*, 2005, **97**(3), 034109.

43 D. M. Marincel, S. Jesse, S. V. Kalinin and L. Q. Chen, Influence of a single grain boundary on domain wall motion in ferroelectrics, *Adv. Funct. Mater.*, 2014, **24**(10), 1409–1417.

44 N. Sun, H. Liu, X. Zhang and Y. Wang, Giant energy-storage density and high efficiency achieved in $(Bi_{0.5}Na_{0.5})TiO_3$–$Bi(N_{0.5}Zr_{0.5})O_3$ thick films with polar nanoregions, *J. Mater. Chem. C*, 2018, **6**(40), 10693–10703.

45 M. Zhou, Y. Li, X. Wang and J. Zhang, Novel $BaTiO_3$-based lead-free ceramic capacitors featuring high energy storage density, high power density, and excellent stability, *J. Mater. Chem. C*, 2018, **6**(31), 8528–8537.

46 Y. Su, N. Liu and G. J. Weng, A phase field study of frequency dependence and grain-size effects in nanocrystalline ferroelectric polycrystals, *Acta Mater.*, 2015, **87**, 293–308.

47 N. Sun, H. Liu, X. Zhang and Y. Wang, High energy-storage density under low electric field in lead-free relaxor ferroelectric film based on synergistic effect of multiple polar structures, *J. Power Sources*, 2020, **448**, 227457.

48 J. P. B. Silva, A. M. R. Lopes, S. S. Dias and R. F. M. Castro, Resistive switching in ferroelectric lead-free $0.5Ba(Zr_{0.2}Ti_{0.8})O_3$–$0.5(Ba_{0.7}Ca_{0.3})TiO_3$ thin films, *J. Phys. D: Appl. Phys.*, 2016, **49**(33), 335301.

49 L. Pintilie, M. Lisca and M. Alexe, Polarization reversal and capacitance–voltage characteristic of epitaxial $Pb(Zr,Ti)O_3$ layers, *Appl. Phys. Lett.*, 2005, **86**(19), 1900698.

50 J. P. B. Silva, M. C. S. Santos, D. F. M. Cardoso and E. R. A. Costa, Wake-up free ferroelectric rhombohedral phase in epitaxially strained ZrO_2 thin films, *ACS Appl. Mater. Interfaces*, 2021, **13**(43), 51383–51392.

51 J. P. B. Silva, M. C. S. Santos, D. F. M. Cardoso and E. R. A. Costa, Ferroelectric switching dynamics in $0.5Ba(Zr_{0.2}Ti_{0.8})O_3$–$0.5(Ba_{0.7}Ca_{0.3})TiO_3$ thin films, *Appl. Phys. Lett.*, 2018, **113**(8), 082903.

52 M. Vasiljevic, J. P. B. Silva, R. M. Oliveira and P. R. G. Souza, Tunable ferroionic properties in CeO_2/$BaTiO_3$ heterostructures, *ACS Appl. Mater. Interfaces*, 2024, **16**(38), 50679–50689.

53 B. Peng, Q. Zhang, X. Li, T. Sun, H. Fan, S. Ke, M. Ye, Y. Wang, W. Lu, H. Niu, J. F. Scott, X. Zeng and H. Huang, Giant electric energy density in epitaxial lead-free thin films with coexistence of ferroelectrics and antiferroelectrics, *Adv. Electron. Mater.*, 2015, **1**, 1500052.

54 Y. Zhang, L. Wang, M. Chen and J. Li, Enhanced energy storage properties and good stability of novel $(1-x)Na_{0.5}Bi_{0.5}TiO_{3-x}Ca(Mg_{1/3}Nb_{2/3})O_3$ relaxor ferroelectric ceramics prepared by chemical modification, *J. Mater.*, 2024, **10**(4), 770–782.

55 L. Wu, H. Zheng, F. Huang and Q. Li, Significantly enhanced dielectric breakdown strength of ferroelectric energy-storage ceramics via grain size uniformity control: Phase-field simulation and experimental realization, *Appl. Phys. Lett.*, 2020, **117**(21), 212902.

56 B. Li, Q. X. Liu, X. G. Tang, T. F. Zhang, Y. P. Jiang, W. H. Li and J. Luo, Antiferroelectric to relaxor ferroelectric phase transition in PbO-modified $(Pb_{0.97}La_{0.02})(Zr_{0.95}Ti_{0.05})O_3$ ceramics with a large energy-density for dielectric energy storage, *RSC Adv.*, 2017, **7**, 43327–43334.

57 M. D. Nguyen, H. T. Vu, Q. V. Tran and T. H. Pham, Relaxor-ferroelectric thin film heterostructure with large imprint for high energy-storage performance at low operating voltage, *Energy Storage Mater.*, 2020, **25**, 193–201.

58 M. Acharya, S. B. Patel, R. P. Singh and V. M. Subramanian, Exploring the $Pb_{1-x}Sr_xHfO_3$ system and potential for high capacitive energy storage density and efficiency, *Adv. Mater.*, 2022, **34**(1), 2105967.

59 C. Yang, M. Zhang, H. Liu and Y. Zhou, Ni doping to enhance ferroelectric, energy-storage, and dielectric properties of lead-free NBT ceramic thin film with low leakage current, *Ceram. Int.*, 2018, **44**(6), 7245–7250.

60 Y. Sun, Y. Zhou, Q. Lu and S. Zhao, High energy storage efficiency with fatigue resistance and thermal stability in lead-free $Na_{0.5}K_{0.5}NbO_3$/$BiMnO_3$ solid-solution films, *Phys. Status Solidi RRL*, 2018, **12**(2), 1700364.

61 Y. Hu, X. Wang, J. Li and S. Zhou, High energy storage performance in lead-free $BiFeO_3$–$BaTiO_3$ ferroelectric thin film fabricated by pulsed laser deposition, *AIP Adv.*, 2019, **9**(8), 085005.

62 Y. Zhang, H. Wang, J. Zhao and L. Chen, Mn doping to enhance energy storage performance of lead-free 0.7NBT–0.3ST thin films with weak oxygen vacancies, *Appl. Phys. Lett.*, 2017, **110**(24), 243901.

63 P. Chen, X. Huang, S. Zheng and L. Li, Enhanced dielectric and energy-storage properties in $BiFeO_3$-modified $Bi_{0.5}(Na_{0.8}K_{0.2})_{0.5}TiO_3$ thin films, *Ceram. Int.*, 2017, **43**(16), 13371–13376.

64 S. Wu, Y. Zhang, H. Wang and X. Chen, Enhanced piezoelectricity and energy storage performances of Fe-doped BNT–BKT–ST thin films, *Ceram. Int.*, 2018, **44**(17), 21289–21294.

65 W. Xu, Q. Li, Y. Liu and Z. Zhang, Spectroscopic study of phase transitions in ferroelectric $Bi_{0.5}Na_{0.5}Ti_{1-x}Mn_xO_{3-\delta}$ films with enhanced ferroelectricity and energy storage ability, *J. Alloys Compd.*, 2018, **768**, 377–386.

66 T. M. Correia, R. L. Withers, M. R. S. Dias and A. K. Singh, A lead-free and high-energy density ceramic for energy storage applications, *J. Am. Ceram. Soc.*, 2013, **96**(9), 2699–2702.

67 B. Luo, X. Wang, Y. Li and Z. Chen, Large recoverable energy density with excellent thermal stability in Mn–modified $NaNbO_3$–$CaZrO_3$ lead-free thin films, *J. Am. Ceram. Soc.*, 2018, **101**(8), 3460–3467.